High charge carrier mobility in solution processed one-dimensional lead halide perovskite single crystals and their application as photodetectors

Tianjun Liu,[a,b] Weidong Tang,[a,b] Sally Luong[a,b] and Oliver Fenwick[a,b]

[a] School of Engineering and Material Sciences, Queen Mary University of London, Mile End Road, E1 4NS, UK.

[b] The Organic Thermoelectrics Laboratory, Materials Research Institute, Queen Mary University of London, Mile End Road, London, E1 4NS, UK.

Abstract

Organic inorganic hybrid metal halide perovskites have emerged as promising candidates for photovoltaics and light-emitting diodes. Recently, interest has been growing in the properties of low-dimensional metal halide perovskites, and one-dimensional versions with strong quantum confinement have demonstrated highly efficient broadband luminescence. Nevertheless, the charge transport mechanism in these low dimensional perovskites remains unclear. In this work, we characterised the charge mobility in one-dimensional perovskite single crystals using a space charge limited current method. Temperature dependent charge mobility measurements indicated that localized polarons at high temperature are replaced by delocalized polarons at low temperature with extended states in the polaronic band. A minimum mobility of 4.51 cm^2/Vs was measured at room temperature. UV photodetectors based on these crystals show an ultrahigh photoresponsivity of 132.3 A W^{-1}. These findings show the promise of high mobility low dimensional perovskite materials for optoelectronic applications.

Introduction

Organic-inorganic hybrid metal halide perovskites have emerged as strong candidates for photovoltaics (PV) with efficiency above 25% in recent years.[1-3] The traditional three-dimensional (3D) perovskite structure, with a cation in the centre of metal halide octahedra, can achieve performance that rivals silicon PV in many respects through tuning of composition,[4] charge transport layer optimization[5] and interface passivation.[6] Two-dimensional (2D) layered perovskite structures can be formed by inserting organic layers between metal halide layers, and these exhibit improved air stability to oxygen and water.[7-9] One-dimensioanl (1D) organo-metal halide perovskite structures, comprised of chains of metal halide octahedra surrounded by organic cations, enrich the structural family of metal halide perovskites and enable applications in light emission with photoluminescence quantum efficiency around 20%.[10, 11] However, the charge transport properties of these low-dimensional perovskite crystals remain relatively unexplored. Fundamental understanding of the charge transport physics of hybrid halide perovskites with low-dimensional structure is important for advancing their applications in high performance optoelectronic devices.

Here, we report temperature dependent space charge limited current (SCLC) measurements on 1D perovskite single crystals. High quality needle-like single crystals were synthesized then structurally characterised by X-ray diffraction (XRD) and transmission electron microscopy (TEM). Furthermore, we fabricated a two terminal device across needle-like 1D crystals and performed in-plane SCLC measurement. Minimum mobilities of 4.51 cm^2/Vs at 300 K and 9.22 cm^2/Vs at 120 K were extracted. In this temperature range we also observe that the intrinsic

charge carrier mobility follows an inverse power law temperature dependence, $\mu \propto T^{-n}$, with

n = 2.04 (120 K to 140 K) and 1.54 (150 K to 200 K). The power exponent close to 3/2 strongly

indicates that the band-like transport is dominated by acoustic phonon scattering in this

temperature range.[12, 13] At higher temperatures mobility increases with temperature, indicating

thermally activated transport. A polaron model is used to explain the charge transport

characteristics where small localized polarons at high temperature change to large delocalized

polarons at low temperature with extended states in the polaronic band.[14]

Results and Discussion

Figure 1a shows the crystal growth process by anti-solvent assisted crystallization (ASC),

which has been widely used in the literature to grow many halide perovskite crystals.[15, 16] In

this work we used a modified version of a reported method.[10] N, N'-dimethylethylenediamine

(DME) (1 mmol) was used as the organic component which was combined with lead bromide

(PbBr$_2$) (1mmol) in hydrobromic acid (HBr) aqueous solution (47 - 49%, 10 ml) and heated to

100 $^{\circ}$C. A transparent solution was obtained after 2 hours of stirring. A vial containing 2 ml of

this precursor solution was placed in a sealed bottle containing 1.5 ml acetone at room

temperature. The elongated colourless crystals were obtained after 12 hours. Successful crystal

growth with ASC relies on the selection of appropriate solvents according to the solubility of

the perovskite and precursor materials. During the process, the antisolvent vapour slowly

diffuses into the inner vial, which gradually reduces the solubility of the perovskite crystals and

the nucleation process occurs once a supersaturation state is reached. Figure 1(b-d) presents

polarized optical microscopic (POM) images of as-grown millimetre-size crystals. The

changing brightness of the crystals with polarization direction is the first indication of a strong anisotropy within the crystals.

Figures 2a and 2b show the crystal structure determined by using single crystal X-ray diffraction at 100 K and refined by SHELXTL. The inorganic lead bromide [$PbBr_4^{2-}$] octahedra share edges in a long chain structure, with the organic DME^{2+} cations forming columnar cages surrounding the inorganic chains. As shown in figure 2c, two main peaks are present at $2\theta =$ 8.75°, 24.55°, corresponding to (101) and (004) planes respectively of the 1D (DME)$PbBr_4$ orthorhombic unit cell. The main peak positions are consistent with reported values (simulated and experimental),[10] whilst none of the crystals show the characteristic peak of lead bromide ($PbBr_2$) at 12.5° [We note that there is a small peak at 12.25º that can be assigned to the (021) plane of the 1D crystal]. In Figure 2d, scanning electron microscopy (SEM) reveals the crack-free morphology of the (DME)$PbBr_4$ crystals over millimetre lengthscales, which enabled us to fabricate single crystal optoelectronic devices (*vide infra*). Figure 2e shows a transmission electron microscopy (TEM) image of the microscale 1D crystals, with the selected area electron diffraction (SAED) pattern shown in Figure 2f. Single points in the SAED patterns representing the (002) and (121) planes can be clearly assigned, which confirms the high quality of our 1D (DME)$PbBr_4$ crystals. This remarkable 1D structure can be described as the self-assembly of inorganic chains that will be responsible for the electronic conductivity within insulating organic shells. The lead bromide chains are composed of double edge-sharing [$PbBr_6^{2-}$] octahedra, which is a bonding environment that differs significantly from the typical corner-shared octahedral in 3D perovskite crystals, such as methylammonium lead bromide (MAPbBr$_3$,

synthesis detailed in supporting information).[17] It is therefore informative to investigate the chemical states of lead and nitrogen in 1D and 3D perovskite structures by X-ray photoelectron spectroscopy (XPS). N 1s and Pb 4f core-level spectra of 1D (DME)PbBr$_4$ and 3D MAPbBr$_3$ perovskite crystals are shown in Figure 3 (a – f). The fitted N 1s peaks (N 1s: 401.67 eV) have a large energy shift of 0.8 eV compared to 3D MAPbBr$_3$ perovskites (N 1s: 402.48 eV). Moreover, there is an additional peak at 399.31 eV presented in Figure 3c, which is probably due to the double ammonium in DME^{2+} clusters. The line shape of Pb 4f spectrum of 1D crystals is broader compared with the Pb 4f spectrum of MAPbBr$_3$ as shown in Figure 3d. The fitted Pb 4$f_{7/2}$ peak of (DME)PbBr$_4$ has components at 138.89 eV, 140.98 eV. Meanwhile, in MAPbBr$_3$ perovskites, the Pb 4$f_{7/2}$ peak appears at 138.38 eV. In traditional 3D hybrid organic-inorganic perovskites, the inorganic octahedra are typical corner-shared. However, the inorganic octahedra are double edge-sharing forming a 1D long chain (often referred to as a quantum wire).[10] In 1D perovskite structures, the fitted Pb 4f spectrum is composed of doublets which are distinct from Pb 4f singlet in 3D MAPbBr$_3$. The difference between them should arise from the different bonding environment on octahedral [PbBr$_6$ $^{2-}$], which is consistent with our XRD results.

We further investigate the charge transport mechanism in these 1D perovskite crystals. Tin-based two-dimensional (2D) perovskites have field-effect transistor (FET) mobility of 0.6 cm^2/Vs,[18] and methylammonium lead iodide (MAPbI$_3$) thin film transistors present a FET mobility of 0.5 cm^2/Vs,[19] whilst our own work suggests a Hall mobility in 3D caesium tin iodide (CsSnI$_3$) of up to 70 cm^2/Vs.[20] Space-charge-limited current (SCLC) measurements have also

been widely used in bulk perovskite materials,[21, 22] where the SCLC mobility can be extracted from current-voltage (I-V) curves by the Mott-Gurney (MG) law. Dong et.al extracted a hole-mobility of 164 ± 25 cm^2/Vs in millimetre-size MAPbI$_3$ bulk crystals by SCLC measurement.[21] In their demonstration, a vertical sandwich structure device was established with top and bottom electrodes. This type of device structure is also commonly used in organic semiconductor thin films solar cells to determine the hole and electron mobility.[23, 24]

Normally, there are four characteristic regimes in log-log I-V curves of these structures: 1) an Ohmic regime where $I \propto V^n$ with n = 1; 2) an SCLC region where Childs law is obeyed with n = 2, but this region is limited by the trap states and the extracted mobility is low; 3) the trap-filled region with n ≥ 3; 4) the trap-free SCLC region with n = 2 where all the traps have been filled and the extracted mobility is higher than in region 2). For the ideal case of trap-free, defect-free single crystals, the mobility can be extracted from Child's law region where $I \propto V^n$ (n = 2). However, for most semiconductor materials, n is between 2 and 3 in region 4). Boer demonstrated a conservative method[25] to extract the minimum SCLC mobility, μ_{min}, for Child's law:

$$\mu_{min} = \frac{8IL^3}{9A\varepsilon_0\varepsilon_r V^2} \qquad \text{Equation 1,}$$

Where a vertical sandwich device was tested with an electrode area, A. L is the length of the channel (defined by the device thickness in this case), ε_0 is the vacuum permittivity, ε_r is relative dielectric constant of the material. The value of the current measured at the maximum applied voltage is used to calculate μ_{min} from equation 1. From de Boer's work on tetracene single

crystals,[25] the observed rapidly increasing current terminates by crossing over into a quadratic regime, therefore the calculated μ_{min} from the maximum voltage in the quadratic approximation is smaller than the intrinsic mobility. This conservative estimation method gives us a reliable value to study the charge transport mechanism in the materials.

In our case, we investigated the charge transport in a planar two-terminal structure for SCLC measurement of low dimensional 1D crystals (Figure 4a). Charge transport was measured in the in-plane direction between two electrodes under an applied bias. The planar SCLC measurement was first demonstrated by Grinberg et al.,[26] showing a relationship between current, I, and voltage, V, which can be described by:

$$I = W \frac{\varepsilon_r \varepsilon_0 \mu V^2}{L^2} \qquad \text{Equation 2,}$$

where W is the width of the channel (defined by the crystal dimension in this case) and μ is the charge-carrier mobility for either electrons or holes. Combining the conservative mobility estimation method and equation 2, we can describe μ_{min} in planar SCLC devices as:

$$\mu_{min} = \frac{IL^2}{W \varepsilon_r \varepsilon_0 V^2} \qquad \text{Equation 3.}$$

To fabricate our 1D single-crystal devices, we first modified SiO_2/Si substrates with a self-assembled monolayer of octadecyltrichlorosilane (OTS), before transferring the crystals onto the surface. Then the substrate with crystals was transferred to a vacuum chamber to remove the residual solvent and to make a good contact between crystals and substrate surface. Top gold contacts (80 nm) were thermally deposited at 5×10^{-7} mbar through a shadow masks with

channel length of 800 μm. Then the devices were then transferred to a Lakeshore probe station connected to a semiconductor parameter analyser (Keithley 4200). As shown in Figure 4b, we investigate the SCLC characteristics at room temperature. In a small voltage range from 0 V to 5 V, the I-V curve shows resistive characteristic with $I \propto V$. With increasing bias, the charge carrier concentration induced by electric field becomes larger than the intrinsic carrier concentration, and the current characteristics switch to SCLC. From 5V to 18 V, a trap limited region is observed ($I \propto V^n$ with n > 3; n=3.2 in our case). Notably, an approximately quadratic curve appears above 20 V (Figure 2b). The minimum SCLC mobility, $\mu_{min} = 4.51$ cm^2/Vs, can be extracted with equation 3. To the best of our knowledge, this is the first time that a SCLC mobility has been extracted for low dimensional perovskite crystals.[22, 27-29]

Furthermore, we investigated the temperature dependence of the 1D perovskite single crystal in the temperature range from 120 K to 250 K (Figure 4c, d). When the temperature is < 200 K, the current decreases with increasing temperature, a typical band-like charge transport behaviour. From 210 K to 250 K, the current increases with temperature, indicating a thermally activated electrical conduction in this temperature range. The current at 120 K is one order of magnitude higher than at 200 K. For the thermally activated (hopping) transport region (210 - 250 K), the activation energy (E_a) can be calculated from an Arrhenius fit at each applied voltage (Figure 4e).[30, 31] E_a is 114.4 ± 54.4 meV and 77.6 ± 23.9 meV at 30 V and 60 V, respectively. Within the accuracy of our measurements, there is no obvious trend in the activation energy as a function of voltage. These values of electric conduction activation energy in our low dimensional perovskite single crystals are comparable to those in trap-free organic

semiconductors.[23]

Considering that two transport behaviours exist in one material (hopping at high temperature, and band-like at low temperature), we can use the polaron model to elucidate the charge transport mechanism.[12, 13, 32, 33] In hybrid halide perovskites, charge formation and transport should be considered within soft and ionic lattice structures. Polarons are electrons or holes dressed by polarization of nuclear coordinates. The formation of polarons arises from two fundamental interaction potentials: the long range Coulomb potential (φ^C) between an excess charge and lattice ions, and the short range deformation potential (φ^d) which relates electronic energy to strain. If φ^d dominates, a small polaron will be generated with coherence length smaller than the unit cell parameter. Small polarons are localized to a unit cell with thermally activated hopping transport, i.e. mobility decreasing with increasing temperature ($d\mu/dT < 0$). When φ^C dominates, coherence length is larger than the cell parameter, resulting large polarons. Large polarons are delocalized among several unit cells with coherent band-like transport, that is, $d\mu/dT > 0$.

Temperature dependence of the minimum SCLC mobility, μ_{min}, from 120 K to 250 K is shown in Figure 5a. From 210 K to 250 K, in the hopping region with thermally activation transport, the extracted activation energy for charge transport from the Arrhenius plot is 78.2 ± 0.05 meV (Figure 5b). We observed two additional temperature regimes identified from the distinct slopes in the minimum SCLC mobility versus temperature plots in the 120 K to 200 K regime (Figure 5c). These have been fitted by a power law, $\mu_{min} \sim \mu_0 T^{-n}$ (n > 0). The exponent, n, is found to be 1.54 ± 0.20 in the temperature range 150 K - 200 K. The power exponent 1.54 (150 K – 200 K) is very close to 3/2, indicating acoustic phonon scattering is dominating in a

coherent band-like transport regime.[12] As temperature decreases below 150 K, the exponent, n, becomes 2.04 ± 0.50, and the mobility has an abrupt increase by a factor of ~ 4 (1.59 cm^2/Vs at 150 K to 6.72 cm^2/Vs at 140 K), which we expect to be due to a phase transition to orthorhombic (orthorhombic phase confirmed at 100 K by single crystal x-ray diffraction, Figure 1(a-c)), which is common for hybrid perovskites in this temperature range.[20] Our data, therefore has found charge transport in 1D perovskite crystals to be consistent with a polaron interpretation, noting that a step increase in polaronic charge carrier mobility at a phase transition has also been observed in MAPbBr$_3$ single crystals.[12]

Photodetectors were fabricated from the 1D perovskite crystals bridged by two electrodes (50 nm gold) on SiO$_2$/Si substrates. Current-voltage curves were recorded in darkness and under 375 nm laser illumination (Figure 6a). We calculated photoresponsivity (R) and gain (G) from the equations below:[15, 34]

$$R = \frac{I_{light} - I_{dark}}{PS} \tag{4}$$

$$G = \frac{(I_{light} - I_{dark})/e}{PS/h\upsilon} \tag{5}$$

Where I_{light} and I_{dark} are the current under illumination and in the dark, respectively. P is the incident power density, S is the effective area being illuminated, $h\upsilon$ is the energy of the incident photon and e is the electronic charge. As shown in Figure 6b, the 1D perovskite single crystal based photodetector shows a high responsivity of 132.3 A W^{-1} and a high gain of 437.3 at a bias of 20 V under 1μ W cm^{-2} illumination. For a photodetector based on perovskite single crystals, rapid response to optical signal is crucial. As shown in the Supporting Information,

the photodetector has ON and OFF times of $\leq$ 105 ms and $\leq$ 117 ms, respectively. True values may be somewhat lower as we were at the time resolution limit of our current measurement system. The time-dependent response of our photodetectors is presented in Figure 6c and Figure S3. The ON and OFF states maintain stable current levels over many cycles under illumination with power density of 2 mW cm^{-2}.

Conclusion

In conclusion, our work sheds light on probing intrinsic charge transport of low dimensional halide perovskite single crystals, with wider implications for the development of hybrid perovskites in photovoltaics, thin film transistors and light-emitting diodes. We have conducted anti-solvent assisted solution synthesis of high quality one dimensional perovskite crystals, which were incorporated into electrical devices, revealing charge transport mechanism. We further characterised the chemical states of N 1s and Pb 4f in this 1D structures by XPS, where the double-edge shared Pb-Br cages is indicated by a Pb 4f peak that is distinct from that found for 3D corner-sharing perovskite cages. Beyond this, we established an in-plane two-terminal SCLC measurement of minimum mobility based on single crystals. Hopping transport dominates at high temperature (210 K to 250 K), while in the low temperature region (120 K to 200 K), band-like transport is observed, obeying the relationship $\mu \propto T^{-n}$ with n = 2.04 $\pm$ 0.50 (120 K to 140 K) and n= 1.54 $\pm$ 0.20 (150 K to 200 K). n $\approx$ 3/2 indicates that coherent band-like transport is limited by acoustic phonon scattering. Polarons in this low dimensional crystal structures therefore dominate charge transport, with small polarons at high temperature becoming larger delocalized polarons at low temperature with extended states in the polaronic

band. UV photodetectors based on these crystals show an ultrahigh photoresponsivity of 132.3 A W^{-1}. These results are important in developing photovoltaic and LEDs applications with enhanced performance based on high mobility low dimensional hybrid perovskites.

Conflicts of interest

The authors declare no competing financial interest.

Reference

1. A. Kojima, K. Teshima, Y. Shirai and T. Miyasaka, *J. Am. Chem. Soc.*, 2009, **131**, 6050-6051.

2. M. M. Lee, J. Teuscher, T. Miyasaka, T. N. Murakami and H. J. Snaith, *Science*, 2012, **338**, 643-647.

3. J. Burschka, N. Pellet, S. J. Moon, R. Humphry-Baker, P. Gao, M. K. Nazeeruddin and M. Gratzel, *Nature*, 2013, **499**, 316-319.

4. N. J. Jeon, J. H. Noh, Y. C. Kim, W. S. Yang, S. Ryu and S. I. Seok, *Nat. Mater.*, 2014, **13**, 897-903.

5. N. J. Jeon, H. Na, E. H. Jung, T. Y. Yang, Y. G. Lee, G. Kim, H. W. Shin, S. I. Seok, J. Lee and J. Seo, *Nat. Energy*, 2018, **3**, 682-689.

6. M. Abdi-Jalebi, Z. Andaji-Garmaroudi, S. Cacovich, C. Stavrakas, B. Philippe, J. M. Richter, M. Alsari, E. P. Booker, E. M. Hutter, A. J. Pearson, S. Lilliu, T. J. Savenije, H. Rensmo, G. Divitini, C. Ducati, R. H. Friend and S. D. Stranks, *Nature*, 2018, **555**, 497-501.

7. J. Z. Song, L. M. Xu, J. H. Li, J. Xue, Y. H. Dong, X. M. Li and H. B. Zeng, *Adv. Mater.*, 2016, **28**, 4861-4869.

8. L. T. Dou, A. B. Wong, Y. Yu, M. L. Lai, N. Kornienko, S. W. Eaton, A. Fu, C.

G. Bischak, J. Ma, T. N. Ding, N. S. Ginsberg, L. W. Wang, A. P. Alivisatos and P. D. Yang, *Science*, 2015, **349**, 1518-1521.

9. F. Zhang, D. H. Kim, H. P. Lu, J. S. Park, B. W. Larson, J. Hu, L. G. Gao, C. X. Xiao, O. G. Reid, X. H. Chen, Q. Zhao, P. F. Ndione, J. J. Berry, W. You, A. Walsh, M. C. Beard and K. Zhu, *J. Am. Chem. Soc.*, 2019, **141**, 5972-5979.

10. Z. Yuan, C. K. Zhou, Y. Tian, Y. Shu, J. Messier, J. C. Wang, L. J. van de Burgt, K. Kountouriotis, Y. Xin, E. Holt, K. Schanze, R. Clark, T. Siegrist and B. W. Ma, *Nat. Commun.*, 2017, **8**.

11. C. K. Zhou, Y. Tian, M. C. Wang, A. Rose, T. Besara, N. K. Doyle, Z. Yuan, J. C. Wang, R. Clark, Y. Y. Hu, T. Siegrist, S. C. Lin and B. W. Ma, *Angew. Chem. Int. Edit.*, 2017, **56**, 9018-9022.

12. H. T. Yi, X. X. Wu, X. Y. Zhu and V. Podzorov, *Adv. Mater.*, 2016, **28**, 6509-6514.

13. K. Miyata, T. L. Atallah and X. Y. Zhu, *Sci. Adv.*, 2017, **3**.

14. T. Holstein, *Ann. Phys. New York*, 2000, **281**, 706-724.

15. X. Zhao, T. Liu, X. Hou, Z. Liu, W. Shi and T. J. S. Dennis, *J. Mater. Chem. C*, 2018, **6**, 5489-5496.

16. X. Zhao, T. Liu, W. Shi, X. Hou, Z. Liu and T. J. S. Dennis, *J. Phys. Chem. C*, 2018, **122**, 8822-8828.

17. E. Edri, S. Kirmayer, M. Kulbak, G. Hodes and D. Cahen, *J. Phys. Chem. Lett.*, 2014, **5**, 429-433.

18. C. R. Kagan, D. B. Mitzi and C. D. Dimitrakopoulos, *Science*, 1999, **286**, 945-947.

19. S. P. Senanayak, B. Y. Yang, T. H. Thomas, N. Giesbrecht, W. C. Huang, E. Gann, B. Nair, K. Goedel, S. Guha, X. Moya, C. R. McNeill, P. Docampo, A. Sadhanala, R. H. Friend and H. Sirringhaus, *Sci. Adv.*, 2017, **3**.

20. T. Liu, S.-Y. Yue, S. Ratnasingham, T. Degousée, P. Varsini, J. Briscoe, M. A. McLachlan, M. Hu and O. Fenwick, *ACS Appl. Mater. Interfaces*, 2019, **11**, 47507-47515.

21. Q. F. Dong, Y. J. Fang, Y. C. Shao, P. Mulligan, J. Qiu, L. Cao and J. S. Huang, *Science*, 2015, **347**, 967-970.

22. M. I. Saidaminov, A. L. Abdelhady, B. Murali, E. Alarousu, V. M. Burlakov, W. Peng, I. Dursun, L. F. Wang, Y. He, G. Maculan, A. Goriely, T. Wu, O. F.

Mohammed and O. M. Bakr, *Nat. Commun.*, 2015, **6**.

23. M. Nikolka, K. Broch, J. Armitage, D. Hanifi, P. J. Nowack, D. Venkateshvaran, A. Sadhanala, J. Saska, M. Mascal, S. H. Jung, J. K. Lee, I. McCulloch, A. Salleo and H. Sirringhaus, *Nat. Commun.*, 2019, **10**.

24. G. Z. Zuo, M. Linares, T. Upreti and M. Kemerink, *Nature Materials*, 2019, **18**, 588-593.

25. R. W. I. de Boer, M. Jochemsen, T. M. Klapwijk, A. F. Morpurgo, J. Niemax, A. K. Tripathi and J. Pflaum, *J. Appl. Phys.*, 2004, **95**, 1196-1202.

26. A. A. Grinberg, S. Luryi, M. R. Pinto and N. L. Schryer, *IEEE T. Electron. Dev.*, 1989, **36**, 1162-1170.

27. D. Shi, V. Adinolfi, R. Comin, M. J. Yuan, E. Alarousu, A. Buin, Y. Chen, S. Hoogland, A. Rothenberger, K. Katsiev, Y. Losovyj, X. Zhang, P. A. Dowben, O. F. Mohammed, E. H. Sargent and O. M. Bakr, *Science*, 2015, **347**, 519-522.

28. A. A. Zhumekenov, M. I. Saidaminov, M. A. Haque, E. Alarousu, S. P. Sarmah, B. Murali, I. Dursun, X. H. Miao, A. L. Abdelhady, T. Wu, O. F. Mohammed and O. M. Bakr, *Acs Energy Lett.*, 2016, **1**, 32-37.

29. Q. F. Han, S. H. Bae, P. Y. Sun, Y. T. Hsieh, Y. Yang, Y. S. Rim, H. X. Zhao, Q. Chen, W. Z. Shi, G. Li and Y. Yang, *Adv. Mater.*, 2016, **28**, 2253-2258.

30. X. M. Zhao, T. J. Liu, Y. T. Zhang, S. R. Wang, X. G. Li, Y. Xiao, X. Y. Hou, Z. L. Liu, W. D. Shi and T. J. S. Dennis, *Adv. Mater. Interfaces*, 2018, **5**.

31. J. W. Wang and C. Jiang, *Org. Electron.*, 2015, **16**, 164-170.

32. J. W. Wang, T. J. Liu, J. Dong, M. L. Li, J. He and C. Jiang, *Small*, 2017, **13**.

33. C. Motta and S. Sanvito, *J. Phys.Chem. C*, 2018, **122**, 1361-1366.

34. M. I. Saidaminov, V. Adinolfi, R. Comin, A. L. Abdelhady, W. Peng, I. Dursun, M. Yuan, S. Hoogland, E. H. Sargent and O. M. Bakr, *Nat. Commun.*, 2015, **6**, 8724.
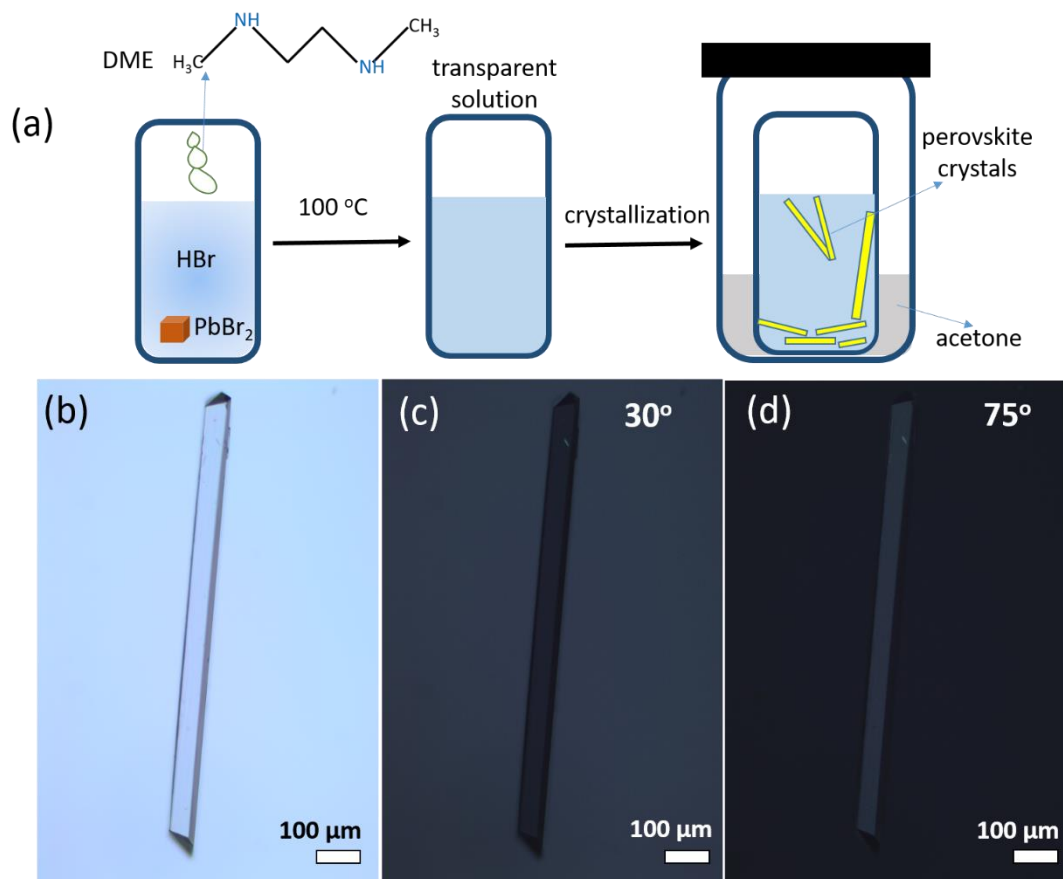
Figure 1. (a) Crystal growth route for (DME)PbBr$_4$ perovskites. (b – d) polarized optical microscopy (POM) of 1D perovskite crystals. Scale bar is 100 μm.
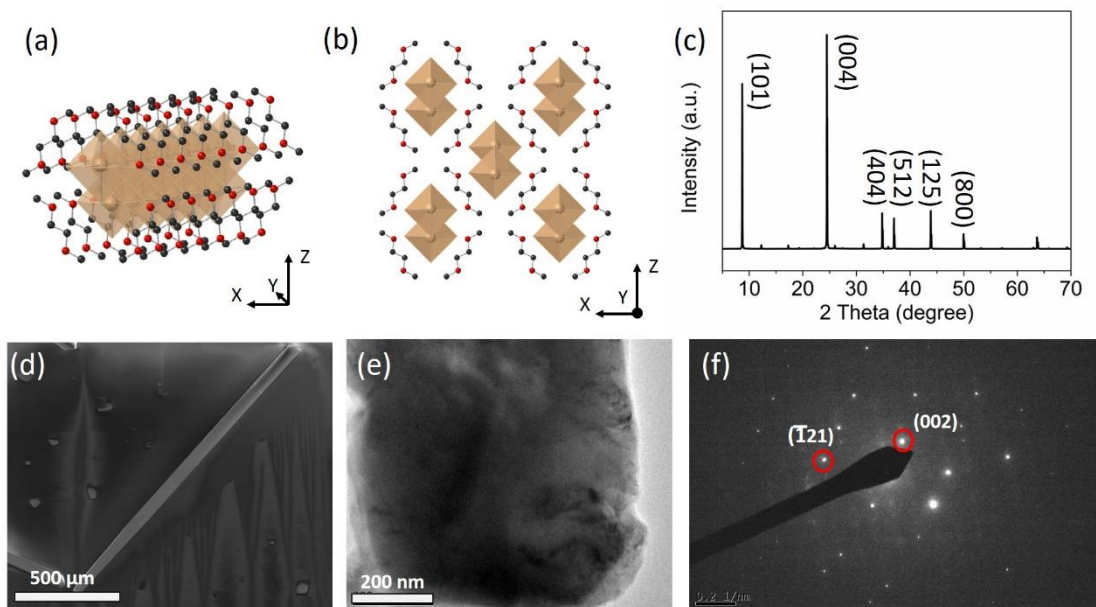
Figure 2. (a), (b) crystal structure of 1D (DME)PbBr$_4$ perovskite crystals. red, black and yellow balls represent N, C and Pb atoms, respectively. (c) Powder X-ray diffraction pattern of 1D crystals. (d) Scanning electron microscopy (SEM) image of 1D crystals with scale bar of 500 μm. (e) Transmission electron microscopy (TEM) image of 1D crystals with scale bar of 200 nm. (f) Selected area electron diffraction (SAED) pattern of the crystal in (e).
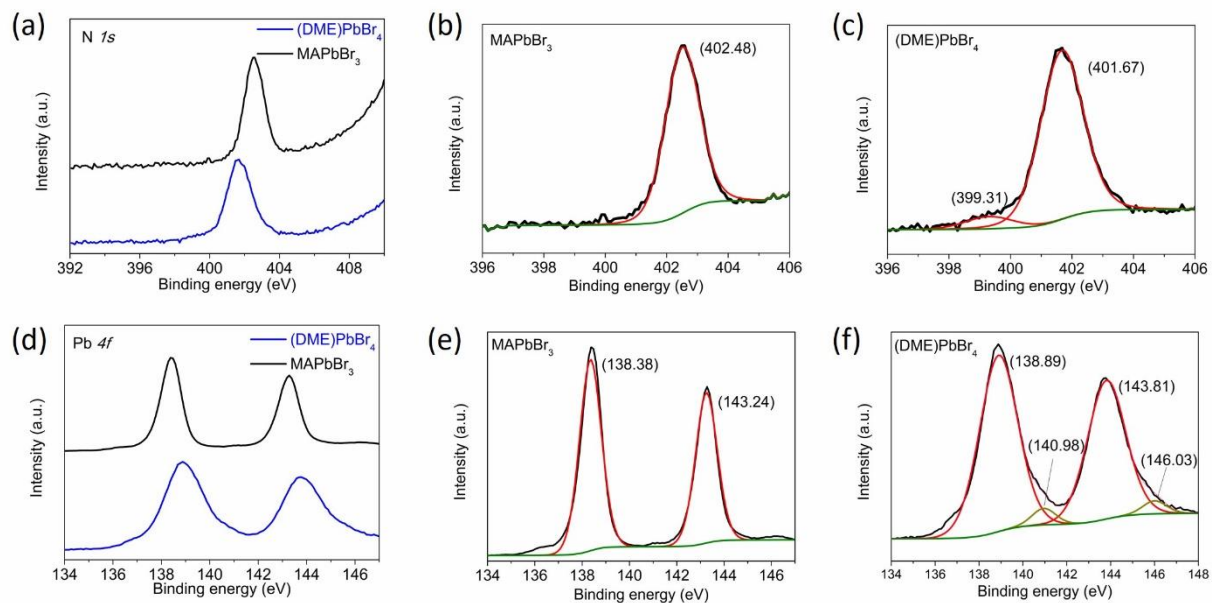
Figure 3. X-ray photoelectron spectroscopy (XPS) analysis. (a) N 1s spectra of (DME)PbBr$_4$ and MAPbBr$_3$ with fitted peaks (b) and (c). (d) Pb 4f spectra of (DME)PbBr$_4$ and MAPbBr$_3$ with fitted peaks (e) and (f). Fitting was performed on the CasaXPS package, incorporating Voigt line shapes and a Shirley background.
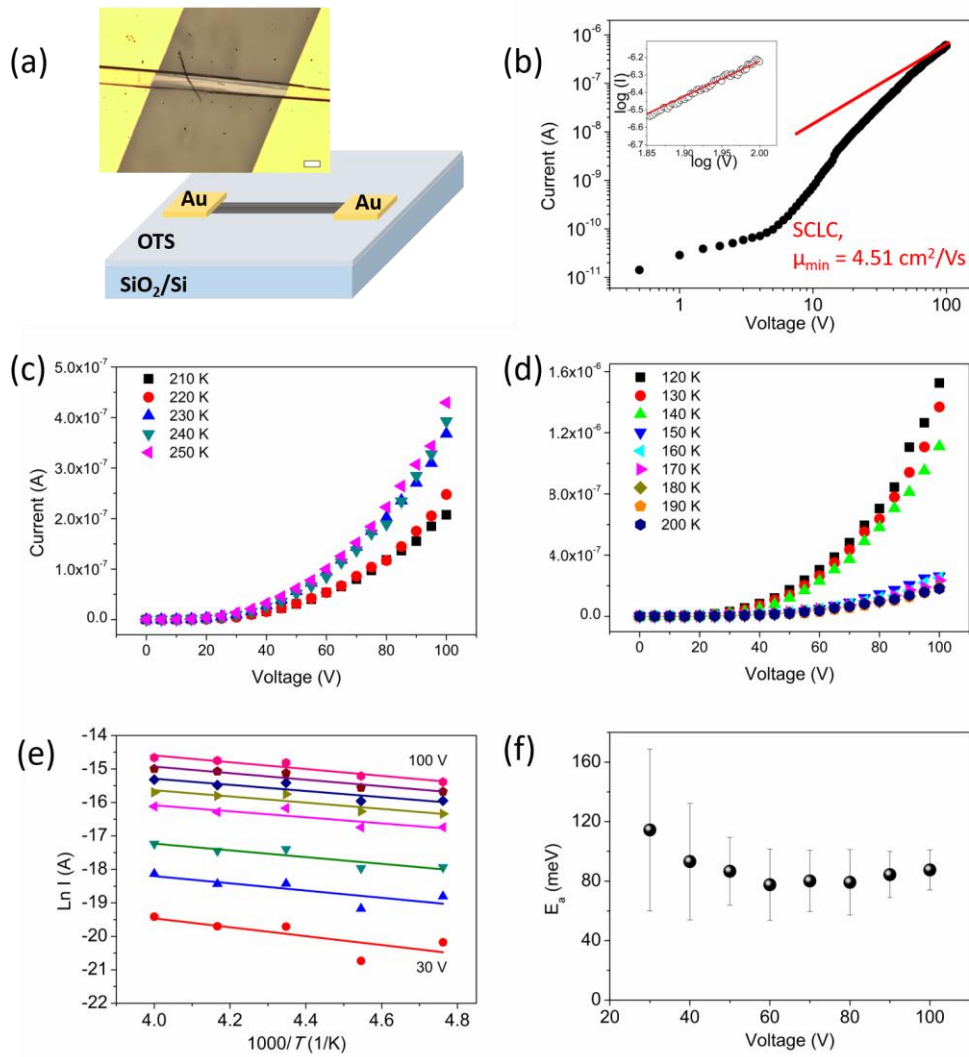
Figure 4. (a) SCLC in-plane measurement structure with two terminal electrodes. Insert image is optical image of device with two terminal gold electrodes. Scale bar is 100 μm. (b) Log-Log I-V characteristics of (DME)PbBr$_4$ crystal devices measured at room temperature from 0 to 100 V. Insert image: a zoom in curve fitting at high voltage. (c), (d) temperature dependence of SCLC I-V characteristics from 210 K to 250 K and 120 K to 200 K, respectively. (e) Arrhenius-type temperature activation of the current for voltage between 30 and 100 V. (f) Extracted activation energy with applied voltage from 30 to 100 V.
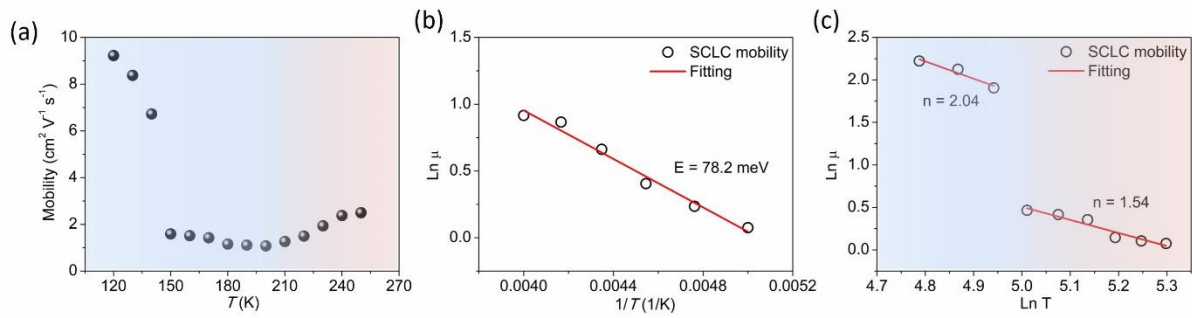
Figure 5. (a) Temperature dependence of minimum SCLC mobility in (DME)PbBr$_4$ perovskite crystals from 120 K to 250 K. (b) Arrhenius-type temperature activation of the charge carrier mobility from 210 K to 250 K.. (c) A double-log plot of temperature dependent SCLC mobility measured at temperature from 120 K to 200 K. Fitted with a power-law dependence $\mu \propto T^{-n}$.
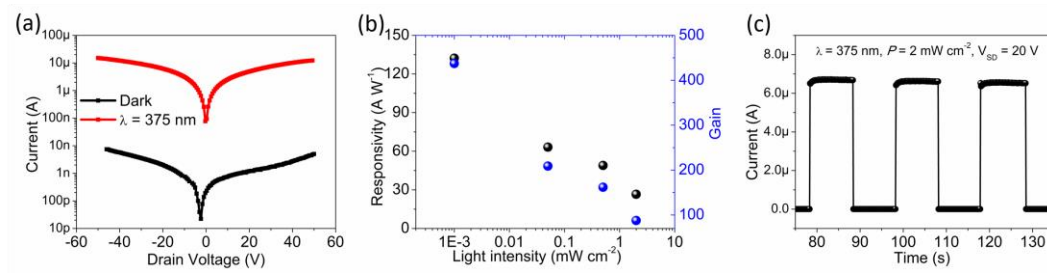
Figure 6 (a) I-V curves of the (DME)PbBr$_4$ photodetectors in darkness and under 375 nm illumination; (b) responsivity and gain vs. light intensity plotted at a bias of 20 V; (c) time-resolved response of the device in darkness and under light.